# Changes in the Vibrational Population of $SO(^3\Sigma^-)$ from the Photodissociation of $SO_2$ between 202 and 207 nm†

**Bogdan R. Cosofret**

*Department of Chemistry and Chemical Biology, Cornell University, Ithaca, New York 14853*

**Scott M. Dylewski**

*School of Applied and Engineering Physics, Cornell University, Ithaca, New York 14853*

**Paul L. Houston***

*Department of Chemistry and Chemical Biology, Cornell University, Ithaca, New York 14853*

*Received: April 3, 2000; In Final Form: June 8, 2000*

Resonance-enhanced multiphoton ionization with time-of-flight product imaging has been used to study the $SO_2 + h\nu \rightarrow SO(^3\Sigma^-) + O(^3P_2)$ channel in the ultraviolet photodissociation of sulfur dioxide at photolysis wavelengths between 202 and 207 nm. These imaging experiments allowed the determination of the vibrational populations of the $SO(^3\Sigma^-)$ fragment at several wavelengths. A change in the vibrational populations occurs from a distribution where most of the population is in $v = 0$ for wavelengths shorter than 203.0 nm to one where the population is more evenly distributed for longer wavelength dissociation. The changes in the internal energy distribution are attributed to participation of two different predissociation mechanisms. Our data suggest that the predissociation mechanism below 203.0 nm involves an avoided crossing with the repulsive singlet state $^1A_1$.

## Introduction

Interest in studying sulfur dioxide comes not only from the fact that it is an important atmospheric trace species, formed primarily from coal combustion, but also from its spectroscopic behavior as a triatomic molecule. The $\tilde{C}\ ^1B_2 \rightarrow \tilde{X}\ ^1A_1$ transition begins around 240 nm as described by Okabe et al.[1] These authors found a sudden decrease in the fluorescence spectrum of this transition from which they deduced that the predissociation threshold lies at approximately 219 nm (5.66 eV), a measurement that is consistent with calculations of the dissociation energy, $D_e = 5.65 \pm 0.01$ eV, estimated using thermochemical data.[2]

The existence of nonadiabatic interactions between the $\tilde{C}\ ^1B_2$ state and neighboring electronic states is well-known, however the predissociation mechanism is not yet completely understood. It seems very likely that the dissociation mechanism changes with wavelength, but the energetic locations of the changes are unknown. Some results suggest that the predissociation mechanism involves an avoided crossing between the $\tilde{C}\ ^1B_2$ state and a repulsive triplet state. Others indicate an avoided crossing of the $\tilde{C}\ ^1B_2$ with a repulsive singlet state, while still other results suggest a mechanism that involves coupling with the ground state. We summarize these arguments below.

**Arguments for Predissociation through Internal Conversion.** Several research groups have concluded that $SO_2$ predissociates through internal conversion to the ground state. Katagiri et al.[3] reviewed most of the previous work on $SO_2$ predissociation from the $\tilde{C}\ ^1B_2$ state and summarized the dissociation rates for both a lower energy region (210−220 nm) and a higher energy region (190−210 nm). They calculated the dissociation rate at 193 nm to be $\sim 4 \times 10^{10}$ s$^{-1}$, corresponding to a lifetime of about 25 ns. This lifetime is longer than the molecular rotation time of 1 ps. Similar rate results were obtained between 210 and 220 nm. They concluded that the dominant dissociation mechanism governing the dissociation rate in the high energy region is not qualitatively different from that in the lower energy region, and they attributed the predissociation mechanism to internal conversion to the ground state, rather than to an avoided crossing between the $\tilde{C}\ ^1B_2$ state and a repulsive state. Katagiri and co-workers also concluded that the singlet mechanism must only be a minor channel, since their potential energy calculations of the $\tilde{C}$ state indicate that the coupling with the singlet repulsive is weak.

Quantum beats observed by Ivanco et al.[4] at the onset of predissociation (218 nm) were attributed to vibronic coupling between the $\tilde{C}$ state and the electronic ground state $\tilde{X}\ ^1A_1$. These authors suggested that the predissociation mechanism might proceed through such coupling with the ground state. Okazaki et al.[5] likewise argued that the predissociation mechanism involves internal conversion to the ground state. Their measurements of the fluorescence lifetime and relative fluorescence quantum yield of the vibronic levels of the $\tilde{C}$ state determined that those levels involving the antisymmetric vibration have larger nonradiative decay rate than other levels. They concluded that the $\upsilon_3$ mode acts as a promoting mode for the nonradiative (predissociation) process. Okazaki et al. also looked at the photofragment yield spectrum of $SO_2$, obtained by monitoring the O atom fragment, and observed that the generation rate of the O atoms coincided with the fluorescence decay rate. Therefore, they concluded that predissociation occurs mainly through the internal conversion to the ground state.

**Arguments for Predissociation through Crossing to a Triplet State.** While many researchers have proposed that the

† Part of the special issue "C. Bradley Moore Festschrift".

10.1021/jp001276w CCC: $19.00 
Published on Web 07/21/2000

predissociation of $SO_2$ proceeds through internal conversion, some experiments suggest a mechanism involving coupling to the nearby $^3A'$ state. On the basis of their infrared diode laser experiments detecting rovibrational transitions of the SO photofragment from $SO_2$ $\tilde{C}$ $^1B_2$ state predissociation at 193 nm, Kanamori et al.[6] hypothesized that $SO_2$ predissociates via the triplet state, at least at this relatively short wavelength. They observed selective population of the $F_1$ and $F_2$ spin components over the $F_3$ spin component and found that over 90% of the nascent SO molecules (70% in $v = 2$ and 20% in $v = 1$) have their electron spin preferentially polarized perpendicular to the molecular axis. From this observation they concluded that crossing to the triplet state must be the dominant channel for predissociation.

Ebata et al.[7] measured the fluorescence excitation spectrum of the $\tilde{C}$ $^1B_2 \rightarrow \tilde{X}$ $^1A_1$ transition at room temperature and in a supersonic free jet in order to understand the role of rotation in the predissociation process. They attributed the difference between the two spectra to the fact that for wavelengths below 219 nm the fluorescence quantum yield from high rotational levels becomes much smaller than that of low rotational levels, indicating a larger predissociation rate in high rotational levels. These results were interpreted in terms of a Coriolis coupling between the $\tilde{C}$ $^1B_2$ state and an assumed triplet repulsive state.

Kawasaki et al.[8] measured the translational energy and angular distributions for the SO photofragments resulting from the 193 nm photodissociation of $SO_2$. They observed an anisotropy of zero, from which they concluded that the dissociation lifetime was greater than the molecular rotation time of 1 ps. The fact that most of the distribution was in high recoil kinetic energies suggests that the dominant dissociation mechanism at 193 nm is through predissociation via crossing with a repulsive state, since most of the energy from the repulsion would then be released as translation between the fragments. The experiment does not provide the multiplicity of the repulsive state.

**Arguments for Predissociation through Crossing to a Singlet State.** Other experimental studies suggest a predissociation mechanism via a singlet repulsive state. Ray et al.[2] looked at dispersed emission spectra at excitation energies near 200 nm, and observed that these are quite different from the dispersed emission spectra found by other researchers at lower excitation energies. This difference may be an indication that the dissociation dynamics change with excitation energy. At low excitation energies (235 and 223 nm), Tzyy-Schiuan and Meyers observed strong progressions in $v_2$ and combinations $v_1 + v_2 v_2$, but very little activity in $v_3$.[9] However, at excitation energies near 210 nm, there is not only evidence for progressions in pure $v_1$ and $v_2$, but also considerable activity in combination bands of these with one quanta in $v_3$. Emission spectra at higher excitation energies (from 198 to 205 nm) show a considerable change; the bands involving $v_1$ become less important as the excitation energy increases, and the bands with odd quanta in $v_3$ become increasingly more important.[2] Transitions involving odd quanta in $v_3$ are nominally forbidden, yet Ray et al. proposed a mechanism by which both the absorption and emission steps could be strongly allowed. The mechanism requires the $A_1$ electronic character of the intermediate state to have a strongly allowed transition via the $a_1$ component of the transition moment to the $A_1$ ground electronic state. Ray et al. argued that this configuration is the repulsive $^1A_1$ state that undergoes an avoided curve crossing with the $\tilde{C}$ $^1B_2$ state.

In summary, data concerning the dissociation mechanism of $SO_2$ seem quite confusing, and it is likely that different mechanisms are operative at different wavelengths. Furthermore, the type of dynamical information that would provide information on the dissociation mechanism is lacking. For example, SO product vibrational distributions have been determined primarily at 193 nm and not at longer wavelengths. Chen, Asmar, Wang, and Weiner[10] measured the nascent vibrational state distributions of $SO(^3\Sigma^-)$ by laser-induced fluorescence spectroscopy and found that the $SO(^3\Sigma^-)$ fragment is produced with an inverted population distribution peaked at the $v = 2$ vibrational level. Similar information was obtained by Felder, Effenhauser, and Huber[11] from time-of-flight (TOF) distributions of SO photofragments: 67% of the populaiton was found to be in the $v = 2$ vibrational level. Finally Kawasaki and Sato[12] also observed that most of the population of the SO fragments is also in $v = 2$, although their vibrational energy distribution is a smoothly varying function which does not have the sharp peak at $v = 2$ as reported by Felder et al. and Chen et al. Without data on the vibrational distributions at other dissociation wavelengths, however, it is difficult to tell how the dissociation mechanism might vary with wavelength or on the vibrational mode of the $SO_2$. In this paper we investigate the predissociation mechanism of the $\tilde{C}$ $^1B_2$ state of $SO_2$ between 202 and 207 nm. By studying the vibrational distribution of the $SO(^3\Sigma^-)$ fragments produced in the $SO_2 + h\nu \rightarrow SO(^3\Sigma^-) + O(^3P_2)$ channel, we seek to understand how the dissociation dynamics depend on either the $SO_2$ mode excited or the photodissociation wavelength.

## Experiment

The technique of ion imaging has been described in more detail elsewhere.[13,14] A 10% $SO_2$/He mixture was expanded at 17 psi through a pulsed 250 $\mu$m diameter nozzle and collimated by a 500 $\mu$m diameter skimmer mounted about 0.5−1.0 cm from the nozzle orifice. Further downstream, the molecular beam was crossed at right angles by two counterpropagating laser beams, one used to dissociate the $SO_2$ and the other to probe the resulting $O(^3P_2)$ fragments using the $O(3p\,^3P_{2,1,0} \leftarrow\leftarrow 2p\ ^3P_2)$ 2+1 REMPI scheme at 225.65 nm.[15,16] Due to the large Doppler width of the $O(^3P_2)$ fragments it was necessary to scan the probe laser over the resonance to ensure that the images detect all product $O(^3P_2)$ atom velocities with equal sensitivity.

The dissociation laser radiation between 202 and 207 nm was produced by doubling the output of a Nd:YAG pumped dye laser (Quanta Ray with a DCM/SR640 dye mixture), and then summing the double light with the fundamental in a BBO crystal (INRAD model AT- II). Typical powers obtained were less than 1 mJ/pulse with a pulse duration of 8−10 ns. The tunable light needed to probe the $O(^3P_2)$ fragments at 225.65 nm was generated by frequency doubling the output of an injection-seeded Nd:YAG-pumped dye laser and then summing the doubled light with the Nd:YAG laser fundamental; typical powers achieved were 2.0 mJ/pulse with a pulse width of 8−10 ns. The photolysis and the probe beams were directed into the vacuum chamber and focused into the interaction region by 25 and 7.5 cm focal length plano-convex lenses, respectively. The dissociation and ionization laser polarizations were parallel to the plane of the detector. The delay time between the pump and probe lasers was set to 17 ns, but the signal was not sensitive to this setting within a reasonable range.

The imaging technique uses an electrostatic immersion lens which serves to extract the ionized $O(^3P_2)$ fragments from the interaction region and to focus ions with equal velocity vectors to the same point on the detector.[17] The magnification factor of this electrostatic lens was measured to be 1.19 ± 0.03 by dissociating $O_2$ at 225.65 nm and detecting the $O(^3P_2)$ fragment using the same REMPI scheme as described above.

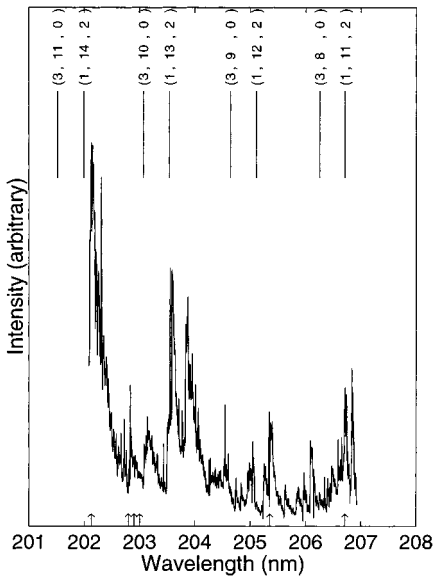


**Figure 1.** Photofragment yield spectra of $SO_2$. The assignments are calculated using first-order anharmonicity and assuming no cross anharmonicities. The assignments are represented as ($\upsilon_1$, $\upsilon_2$, $\upsilon_3$) = (symmetric stretch, bend, asymmetric stretch). The arrows indicate the wavelengths for which images are shown in Figure 2.

The ionized fragments were accelerated into a field-free flight tube mounted along the axis of the molecular beam. The ions were imaged by a position sensitive detector consisting of a chevron double microchannel plate (MCP) assembly (Galileo) coupled to a fast phosphor screen. The image on the screen was recorded by a 640 × 480 pixel CCD camera (Xybion). Both the MCP and the camera were electronically gated to collect signal corresponding only to the mass of the $O(^3P_2)$ fragment. Signal levels were kept below 300 ions per frame to ensure accurate ion counting. Data were accumulated typically for 80 000 total laser shots.

The photofragment yield spectrum of $SO_2$ was obtained by monitoring the $O(^3P_2)$ formation using a photomultiplier tube (Hamamatsu 1P21) mounted near the phosphor screen while scanning the photolysis laser in the region between 202 and 207 nm. The output of the photomultiplier tube was sent to a boxcar averager gated at the appropriate arrival time. Both the probe laser and photolysis powers were measured simultaneously with a photodiode in order to normalize the $O(^3P_2)$ signal intensity for fluctuations in laser power.

## Results

Our experimental efforts have concentrated on the detection of $O(^3P_2)$ fragments formed in the $SO_2 + h\nu \rightarrow SO(^3\Sigma^-) + O(^3P_j)$ photodissociation channel of $SO_2$, probed using a 2+1 REMPI scheme. We have investigated the photolysis at wavelengths between 202 and 207 nm.

We first measured the yield spectrum by monitoring the O atom fragment through the ($3p\ ^3P_J \leftarrow\leftarrow 2p\ ^3P_2$) transition. Figure 1 shows the O atom yield spectrum. Our spectrum serves to extend the LIF spectrum measured earlier by Okazaki et al.[5] between 218 and 207 nm. The mode assignments shown in Figure 1 are based on our extension of their results and are calculated using first-order anharmonicity and assuming no cross anharmonicities.

To understand better the dissociation dynamics of the $\tilde{C}$ state of $SO_2$, images of the velocity distributions of the $O(^3P_2)$ fragments were taken at the wavelengths shown by the small arrows in Figure 1. Since the dissociation lifetime of $SO_2$ is longer than the molecular rotation time, the spatial anisotropy parameter, $\beta$, is expected to be nearly zero.[3,8] The images shown in Figure 2 are slices through the reconstructed three-dimensional distributions of the $O(^3P_2)$ fragments at six photolysis wavelengths: 202.13, 202.80, 202.90, 203.00, 205.35, and 206.71 nm. In these images, the electric vectors of the dissociation and ionization lasers are pointing in the same direction, parallel to the face of the microchannel plate detector and in the vertical direction of Figure 2. Images were also taken with the electric vector of the dissociation light perpendicular to the detector, and, as expected, the angular distributions were identical within experimental error.

The product imaging technique makes use of an inverse Abel transform to reconstruct the three-dimensional velocity distribution from its two-dimensional projection.[13,14] The procedure works well except for products having very small velocities in directions orthogonal to the axis of cylindrical symmetry. To correct for this inverse Abel transform singularity along the vertical axis, the images were altered slightly by fitting the angular distributions to a $[1 + \beta P_2(\cos\theta)]$ distribution and interpolating across the middle 12 pixels for radii greater than 10 pixels.

The $O(^3P_2)$ velocity distributions recovered from the inverse Abel transform slices can be separated into angular and speed components. Angular distributions are determined by integrating over the desired speed interval for each angle, while the speed distribution is achieved in a similar manner by integrating over all angles for each speed. The speed distributions can be further transformed, using the law of conservation of momentum, into total translational energy distributions for $SO_2 \rightarrow SO(^3\Sigma^-) + O(^3P_2)$ dissociation. The vibrational level of the SO fragment is related to the translational energy through conservation of energy:

$$\mathrm{KE} = E_{h\nu} - D_0(\mathrm{SO{-}O}) - E_{\mathrm{SO}}(\upsilon,J) \qquad (1)$$

where $D_0$(SO−O) is the $SO_2$ dissociation energy, 5.65 ± 0.01 eV, to form $SO(^3\Sigma^-) + O(^3P_2)$,[3] and $E_{SO}(\upsilon,J)$ is the SO internal energy. The kinetic energy distributions together with a comb indicating the energy of the vibrational states of the SO fragment formed in conjunction with $O(^3P_2)$ are shown in Figure 3. The major source of error in the energy axis is due to the magnification factor. We measured the magnification factor of our electrostatic lens to be 1.19 ± 0.03. The low signal-to-noise ratio at the wavelengths $\lambda$ = 203.00 nm, $\lambda$ = 202.90 nm and $\lambda$ = 202.80 nm is due to the fact that the total O atom yield is low in this region, as shown in the spectrum of Figure 1.

By obtaining information on the internal energy distribution of the $SO(^3\Sigma^-)$ fragment, one may be able to identify different dissociation dynamics of the $\tilde{C}$ state of $SO_2$. Images similar to those shown in Figure 2 have been taken not only at the wavelengths of every mode assigned in the spectrum of Figure 1, but also at the wavelengths corresponding to some of the valleys. Our objective was to establish whether the dissociation dynamics depended on the mode excited and to learn if there might be a background absorption that gave a different SO internal energy distribution than excitation of the peaks in Figure 1. Our observations indicate that the internal energy of the SO fragment is similarly distributed in peaks or adjacent valleys. However, at the photolysis wavelength of 203.0 nm we observe an interesting change in the internal energy distribution of the SO fragment. For wavelengths greater than 203 nm the distribution is almost evenly distributed between $\upsilon = 0{-}2$ of the SO fragment. Below 203 nm the internal energy is mostly in $\upsilon = 0$ with little population in the other vibrational levels.

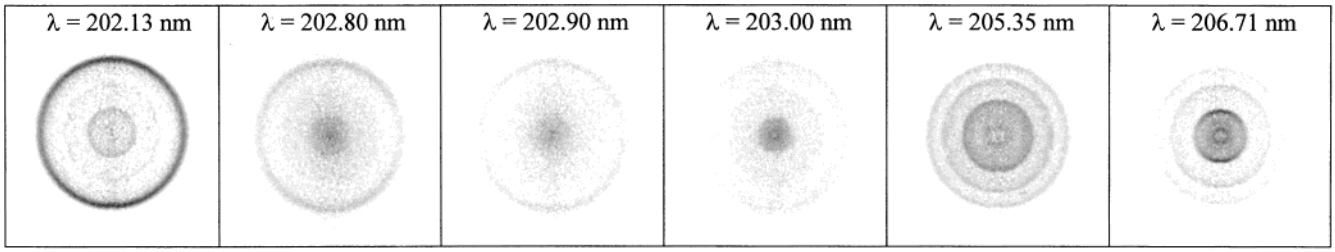


**Figure 2.** Reconstructed 3D distributions of the $O(^3P_2)$ fragments from sulfur dioxide photodissociated at 202.13, 202.80, 202.90, 203.00, 205.35, and 206.71 nm.

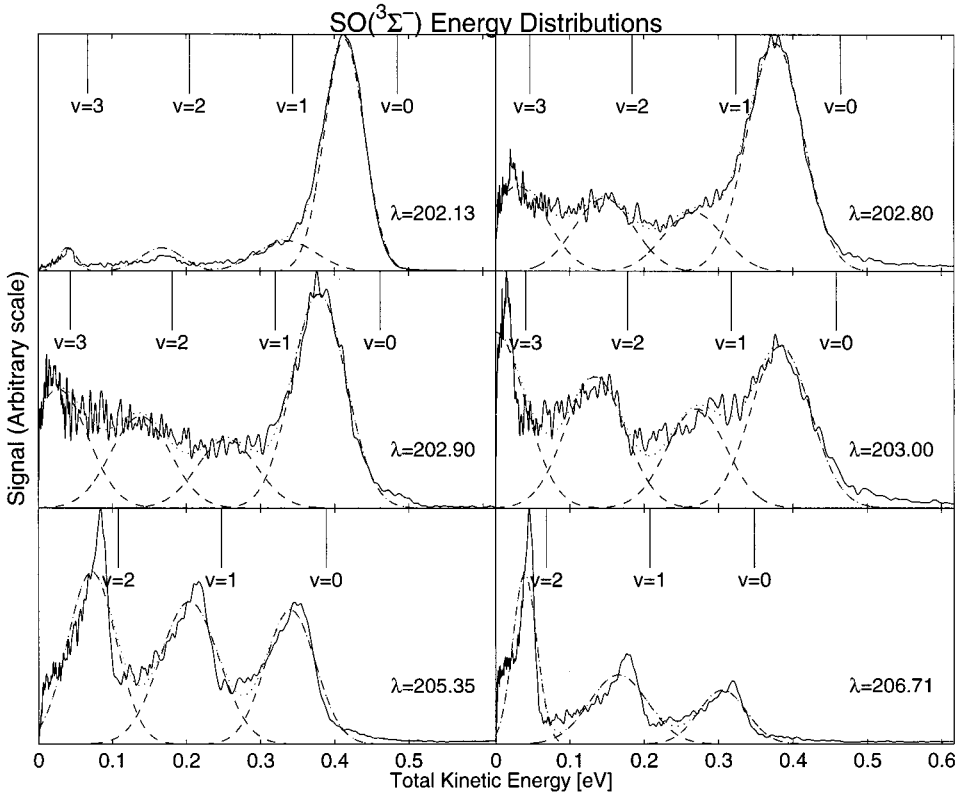


**Figure 3.** The total translational energy distributions for the dissociation of $SO_2$ to $SO(^3\Sigma^-) + O(^3P_2)$ at 202.13, 202.80, 202.90, 203.00, 205.35, and 206.71 nm. The vibrational levels of the $SO(^3\Sigma^-, J = 0)$ fragment are indicated by the combs. The dashed lines are Gaussian fits used to determine the vibrational populations.

**TABLE 1: Percent Populations of the Vibrational Levels of the SO Fragment at Six Different Photolysis Wavelengths**

| wavelength (nm) | % in $v = 0$ | % in $v = 1$ | % in $v = 2$ | % in $v = 3$ |
|---|---|---|---|---|
| 202.13 | $73.7 \pm 5.7$ | $14.7 \pm 1.4$ | $7.9 \pm 3.7$ | $3.6 \pm 1.0$ |
| 202.80 | $51.9 \pm 2.1$ | $14.4 \pm 0.6$ | $17.8 \pm 0.5$ | $15.9 \pm 1.2$ |
| 202.90 | $43.8 \pm 5.5$ | $15.5 \pm 2.0$ | $20.6 \pm 1.3$ | $20.0 \pm 2.1$ |
| 203.00 | $33.7 \pm 2.2$ | $20.7 \pm 0.6$ | $27.3 \pm 0.4$ | $18.3 \pm 2.0$ |
| 205.35 | $28.7 \pm 0.6$ | $35.8 \pm 1.2$ | $35.5 \pm 1.4$ | 0 |
| 206.71 | $23.9 \pm 1.2$ | $37.9 \pm 0.8$ | $38.2 \pm 0.6$ | 0 |

Table 1 shows the population in each vibrational mode of the SO fragment at the six different photolysis wavelengths. The percentages are obtained by integrating Gaussian fits to the overall energy distributions. The major sources of error in the energy distribution plot and thus in the vibrational fits are from the counting statistics and the magnification factor. The counting statistics introduce an error in the intensity of the distributions, while the magnification factor affects the total kinetic energy. By propagating both the magnification factor error and the counting statistics error, we can obtain the error in the energy distributions. The error in the percent population is obtained by fitting Gaussian curves to the energy distributions corresponding to the maximum and minimum variations in the magnification factor and amplitude range. The fitting procedure is an approximation since, as can be seen in Figure 3, the vibrational peaks are not perfect Gaussian forms. There is no population in $v = 3$ of the SO fragment at 205.35 and 206.71 nm because these wavelengths correspond to energies below the threshold for $SO(v = 3)$.

An overview of the internal energy distribution changes with wavelength is given by Figure 4, which shows the relative populations for $v = 0-3$ as a function of photolysis wavelength. It is clear that starting at around 203 nm the populations in all the accessed vibrational levels become more evenly distributed at longer wavelengths.

The imaging data also provides angular information. Close examination of the images in Figure 2 reveals what at first appears to be a slight anisotropy. The literature results indicate that the dissociation lifetime of $SO_2$ is longer than the molecular rotation time and Kawasaki et al.[8] measured an anisotropy of zero at 193 nm. We suspected that the slight anisotropy we observed was due to a possible alignment of the $O(^3P_2)$ fragment rather than to an anisotropic distribution of recoil velocities. To test this hypothesis, we investigated the angular distribution

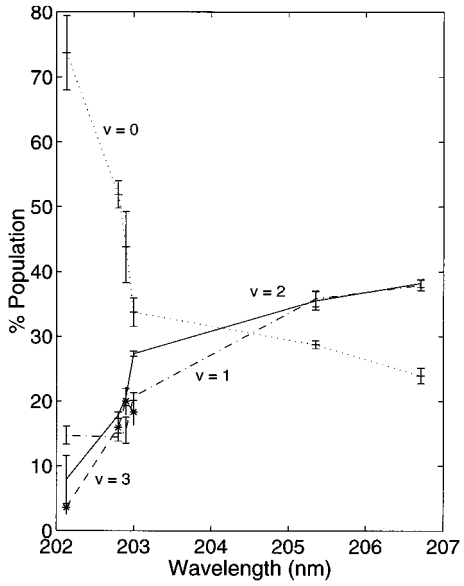


**Figure 4.** Vibrational populations in the SO($^3\Sigma^-$, $v = 0-3$) fragment from the photodissociation of $SO_2$ as a function of wavelength.

for the O($^3P_0$) fragments at 202.13 nm. Because O($^3P_0$) has no rotational angular momentum, it cannot be aligned. For these tests, both the probe and the dissociation laser polarizations were parallel to the plane of the detector. We measured an anisotropy value, $\beta$, where the angular distribution is given as $I(\theta) \propto 1 + \beta P_2(\cos\theta)$ of $-0.04 \pm 0.10$. An error range was assigned for the anisotropy value by the following procedure. At the 202.13 nm photolysis wavelength, four separate images were taken. Each image was then analyzed independently to obtain four separate values for $\beta$, and the spread was used as an error range at that dissociation wavelength. It thus appears that there is no true anisotropy in the images, an observation that indicates that the dissociation is rapid on the time scale of parent rotation.

We also looked at the effects of the polarization direction of the probe laser on the angular distributions for production of O($^3P_2$). Sets of two images were taken at three photolysis wavelengths: 202.13, 203.00, and 206.71 nm, one with polarization vector of the probe laser parallel to the plane of the detector, and the other image with polarization vector perpendicular to the plane of the detector. In both images the electric vector of the dissociation laser was maintained parallel to the plane of the detector. The two images were normalized to contain the same number of total ions and then subtracted in order to show the effects induced by the polarization direction of the probe laser. Figure 5 shows the two images at 202.13 nm along with the subtracted image. Similar studies were done for $\lambda = 203.00$ nm and $\lambda = 206.71$ nm, where we found both that the alignment persisted and also that the qualitative shape of the alignment did not change. We argue below that the deviation of the apparent anisotropies from zero for O($^3P_2$) fragments is due to a $\mathbf{v}-\mathbf{J}$ correlation.

Finally, we measured the ratio of O($^3P_J$) spin−orbit populations at three different wavelengths. At 202.13 nm we found ($^3P_2$):($^3P_1$):($^3P_0$) = (49.6 ± 1.5):(34.5 ± 4.5):(15.6 ± 4.9); at 203.55 nm ($^3P_2$):($^3P_1$):($^3P_0$) = (71.5 ± 4.4):(22.8 ± 3.3):(5.2 ± 2.2); and at 205.34 nm ($^3P_2$):($^3P_1$):($^3P_0$) = (62.8 ± 7.8):(30.2 ± 7.4):(6.0 ± 0.8).

## Discussion

Our data have extended previous $SO_2$ $\tilde{C} \leftarrow \tilde{X}$ assignments based on laser-induced fluorescence to higher energy by monitoring the product yield rather than the fluorescence. In the LIF spectrum described by Okazaki et al.[5] two main progressions have been assigned to the series involving the bending vibration, that is ($\upsilon_1$, $\upsilon_2$, $\upsilon_3$) = (1, $n$, 0) and (3, $n$, 0). Above the dissociation threshold, the assignments are not straightforward due to anharmonic coupling (Fermi resonance and/or Coriolis coupling). Okazaki and co-workers concluded that the bending progression of the (1, $n$, 2) series shows prominent features toward the higher energy region (below 218 nm), and also that the (1, $n$, 2) bands having odd quanta in the bending mode are split into two bands.[5] As has been discussed by Yamanouchi et al.,[18] simple normal mode assignments using the ($\upsilon_1$, $\upsilon_2$, $\upsilon_3$) notation are not entirely appropriate due to strong $\upsilon_1 - 2\upsilon_3$ Fermi resonances in the high vibrational energy region. Our yield data provide information in this higher energy region. Although our assignments, based on those at lower energy, may be inappropriate due to the difficulty involved in using normal modes, the new data do agree with the earlier work in two respects. First, bands with odd quanta in the bending mode display splitting, as it can be seen in Figure 1 for the (1, 11, 2) and (1, 13, 2) bands. Second, the (1, $n$, 2) progression is dominant.

The vibrational populations measured in our experiments as a function of dissociation wavelength indicate that the internal energy distributions of the SO($^3\Sigma^-$) fragments do not depend on the vibrational modes excited, but instead are most sensitive to whether the dissociation is above or below a specific dissociation energy (corresponding to 203.0 nm). This observation may indicate that the predissociation mechanism from the $\tilde{C}$ state changes at this wavelength. In $C_s$ geometry, SO($^3\Sigma$) and O($^3P_2$) can combine to form $SO_2$ in one of two A′ and one A″ states. Since both the SO and O fragments have spin multiplicities of 3, each electronic state of $SO_2$ can have a total spin of 0, 1, or 2 (singlet, triplet, or quintet). The quintets are not considered further because no experimental evidence has been reported about them and because an indirect interaction between such a quintet state and the $\tilde{C}$ $^1B_2$ state is expected to be negligibly small.[3] One of the $^1$A′ states is the ground state of $SO_2$, while the other $^1$A′ is an excited, repulsive state. One of the $^3$A′ states is bound, while the other $^3$A′ is again an excited, repulsive state. Since the $\tilde{C}(^1B_2)$ state of $SO_2$ does not directly correlate to the SO($^3\Sigma^-$) + O($^3P_2$), one way to arrive at the SO($^3\Sigma^-$) + O($^3P_j$) asymptote would be through the avoided crossing of the $\tilde{C}$ state potential energy surface with one of these repulsive states. The avoided crossing pseudoseam between the $\tilde{C}$ ($2^1$A′) state and the singlet ($3^1$A′) repulsive state is at higher energies than the triplet seam, indicating that the predissociation mechanism via the repulsive singlet would occur at higher excitation energies than predissociation via the repulsive triplet.

Katagiri et al.[3] calculated crossing seams between the $\tilde{C}$ state and the repulsive singlet and triplet states by varying the R and $\gamma$ coordinates when one S−O bond length is fixed at $2.706a_0$. The ab initio calculations showed that the bound $\tilde{C}$ $^1B_2$ ($2$ $^1$A′, in $C_s$ geometry) and the repulsive singlet ($3^1$A′) states cross with each other almost diabatically. The two-dimensional potential energy surface calculated by Katagiri et al. shows the interaction between the $\tilde{C}$ state and both the singlet and the triplet repulsive states; please refer to Figure 9 of ref 3. The crossing seams between these states run along the energy contours on the outer wall of the bound potential energy surface of the $\tilde{C}$ state. On the basis of these observations, the authors concluded that the contribution from the dissociation through the mixing with the singlet and the triplet states may be quite small. They attributed the predissociation mechanism instead

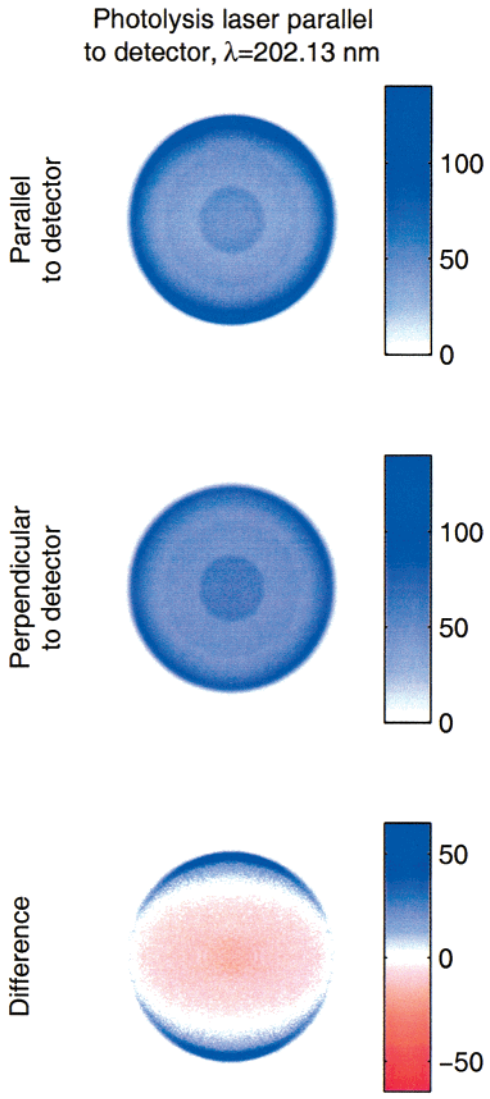


**Figure 5.** O($^3P_2$) images taken at 202.13 nm. The upper and middle images were taken with the ionization laser polarization parallel and perpendicular to the detector face, respectively. These two images were then scaled to contain the same total ion count and subtracted to show the effect of the ionization laser. The subtracted image is presented in the bottom panel.

to an internal conversion in which the vibronic levels of the $\tilde{C}$ state couple with those of the ground electronic state, which correlates to the asymptote SO($^3\Sigma^-$) + O($^3P_2$). However, since the dissociative wave functions on the repulsive states as well as the $\tilde{C}$ state vibrational wave function are seen theoretically to have large amplitudes along the crossing seams,[3] the dissociation via crossing with these repulsive states may have important contributions near the seam crossing energy regions.

For $SO_2$ trajectories that move away from the Franck−Condon point on the potential energy surface calculated by Katagiri et al.,[3] the energy falls steeply into the well, after which the geometry changes to smaller $\gamma$ and larger $R$. This prediction is consistent with our results of Figure 1, where the two main progressions are bending progressions with large quanta in the bending mode. According to Ray et al.,[2] such trajectories would reach the avoided crossing singlet seam at angles near 100°, where Katagiri et al. find that the coupling between the $\tilde{C}$ state and the singlet state is stronger; the splitting between electronic states is as large as 0.1 eV near $\gamma = 90°$. Such a splitting may be large enough to allow the trajectories to evolve adiabatically through the avoided crossing.[2]

The internal energy distribution results we have measured show that at dissociation wavelengths below 203 nm most of the internal energy of the SO($^3\Sigma^-$) fragment is in $v = 0$ (~75%), indicating very little internal energy excitation of the SO($^3\Sigma^-$) fragment. At dissociation wavelengths above 203 nm dissociation, we see a change in the energy distribution such that the internal energy of the SO fragment becomes more evenly distributed in $v = 0$, 1, 2, and 3 (e.g., at 206.71 nm, ~24% in $v = 0$, ~34% in $v = 1$, and ~40% in $v = 2$). Without a change in dissociation mechanism, we would expect the vibrational distribution to evolve smoothly from low vibrational energy at high dissociation wavelengths to increased vibrational energy at shorter wavelengths. Not only does the observed distribution go in the opposite direction from this expectation, it changes abruptly at 203 nm. The abrupt change may indicate the onset of a second predissociation mechanism for the $\tilde{C}$ state of $SO_2$.

The small amount of internal energy present in the SO($^3\Sigma^-$) fragment at dissociation wavelengths lower than 203.0 nm corresponds to high recoil kinetic energy. For example, dissociation at 202.13 nm photodissociation produces almost 75% of the fragments at a kinetic energy of 0.4 eV. This high observed kinetic energy is consistent with crossing from the $SO_2$ $\tilde{C}$ state to a state that is predominantly repulsive in the OS−O dissociation coordinate. Both Katagiri et al.[3] and Ray et al.[2] suggest that the crossing of the $\tilde{C}$ state with the repulsive singlet is sufficiently avoided at some geometries to proceed adiabatically. Our results thus suggest that this channel opens as the dissociation wavelength decreases below 203.0 nm. For wavelengths greater than 203.0 nm, the vibrational population is more evenly distributed among the open product states. It seems reasonable that this distribution comes from a more statistical dissociation following internal conversion to very high vibrational levels of the ground electronic state. However, since some SO($v = 0$) is observed, one cannot rule out a contribution to the dissociation mechanism from the avoided crossing mechanism even at dissociation wavelengths above 203.0 nm.

The conclusion that a new predissociation channel opens at wavelengths below 203 nm is also consistent with the emission spectra excited near 200 nm in the work of Ray et al.,[2] which show strong emission into odd-$v_3$. Such a transition is nominally forbidden, but according to Ray et al. both the emission and absorption steps may become allowed if the $A_1$ electronic character of the intermediate repulsive state were to have strongly allowed transition via the $a_1$ component of the transition moment to the $A_1$ ground electronic state. They proposed that the intermediate state is the singlet repulsive state that undergoes curve crossing with the $\tilde{C}$ state.

Kawasaki et al.[8] measured an anisotropy parameter of $\beta = 0$ at 193 nm, from which they concluded that the lifetime of the $\tilde{C}$ state must be longer than the molecular rotation time of 1 ps. Katagiri et al.[3] also concluded that the lifetime was much longer than the molecular rotation time. Our results examining the O($^3P_0$) fragment support these conclusions, since we also find that $\beta = -0.04 \pm 0.10$. Results for the O($^3P_2$) product indicate a dependence on the polarization of the probe laser, as shown in the difference signal of Figure 5 for dissociation at 202.13 nm. We did not find a similar dependence on the polarization of the probe laser for the O($^3P_0$) product, nor did we expect one since this product has no angular momentum to be aligned. It is important to note that since the $SO_2$ lifetime is long, it is impossible to distinguish between parallel and perpendicular transitions in the $SO_2$ molecule. Theoretically, it should still be possible to determine the $m_j$ distribution of the atomic fragment from our measurements, yet the line strength factors for the

specific O(3p $^3P_J \leftarrow$ 2p $^3P_2$) REMPI transition we used have not been measured and cannot be easily calculated. From the similarity of the alignment at wavelengths above and below 203 nm, however, it appears that the $m_j$ distribution of the atomic fragment does not depend strongly on the dissociation wavelength.

The spin−orbit ratios of the O($^3P_J$) states do show a change above and below 203 nm. Measurably more population in O($^3P_2$) is evident at longer wavelengths than at shorter wavelengths, and the distribution is much flatter at the short wavelengths than at the longer wavelengths. Under the assumption that shorter wavelength dissociation is partly caused by an avoided crossing, the crossing appears to put more population into low-*J* spin−orbit states of the oxygen atom as compared to the dissociation at longer wavelengths.

## Conclusion

The product imaging technique has provided information on the internal energy of the SO($^3\Sigma^-$) fragment as a function of the dissociation wavelength. A sudden change in the distribution at a dissociation wavelength of 203 nm suggests a change in the dissociation mechanism. The anisotropy parameter for $SO_2$ photodissociation has been found to be $\beta = -0.04 \pm 0.10$, indicating that dissociation takes place on a time scale rapid compared to $SO_2$ rotation. However, a dependence of the product images on the polarization of the probe laser indicates that the O($^3P_2$) product is aligned. The O($^3P_J$) population distribution depends weakly on dissociation wavelength.

**Acknowledgment.** We are grateful to Dr. Pat J. Pisano for his help and lively discussions. This work was supported by the National Science Foundation under grant CHE-9901065. This work made use of the Cornell Center for Materials Research Shared Experimental Facilities, supported through the National Science Foundation Materials Research Science and Engineering Centers program (DMR-9632275).

## References and Notes

(1) Okabe, H. *J. Am. Chem. Soc.* **1971**, *93*, 7095−6.
(2) Ray, P. C.; Arendt, M. F.; Butler, L. J. *J. Chem. Phys.* **1998**, *109*, 5221−30.
(3) Katagiri, H.; Sako, T.; Hishikawa, A.; Yazaki, T.; Onda, K.; Yamanouchi, K.; Yoshino, K. *J. Mol. Struct.* **1997**, *413*−*414*, 589−614.
(4) Ivanco, M.; Hager, J.; Sharfin, W.; Wallace, S. C. *J. Chem. Phys.* **1983**, *78*, 6531−40.
(5) Okazaki, A.; Ebata, T.; Mikami, N. *J. Chem. Phys.* **1997**, *107*, 8752−8.
(6) Kanamori, H.; Butler, J. E.; Kawaguchi, K.; Yamada, C.; Hirota, E. *J. Chem. Phys.* **1985**, *83*, 611−14.
(7) Ebata, T.; Nakazawa, O.; Ito, M. *Chem. Phys. Lett.* **1988**, *143*, 31−7.
(8) Kawasaki, M.; Kasatani, K.; Sato, H.; Shinohara, H.; Nishi, N. *Chem. Phys.* **1982**, *73*, 377−82.
(9) Tzyy-Schiuan, Y.; Myers, A. B. *J. Chem. Phys.* **1991**, *95*, 6207−17.
(10) Chen, X.; Asmar, F.; Wang, H.; Weiner, B. *J. Phys. Chem.* **1991**, *95*, 6415−6417.
(11) Felder, P.; Effenhauser, C. S.; Huber, J. R. *Chem. Phsy. Lett.* **1988**, *148*, 417−421.
(12) Kawasaki, M.; Sato, H. *Chem. Phys. Lett.* **1987**, *139*, 585−588.
(13) Wilson, R. J.; Mueller, J. A.; Houston, P. L. *J. Phys. Chem. A* **1997**, *101*, 7593.
(14) Chang, B.-Y.; Hoetzlein, R. C.; Mueller, J. A.; Geiser, J. D.; Houston, P. L. *Rev. Sci. Instrum.* **1998**, *69*, 1665.
(15) Bamford, D. J.; Jusinski, L. E.; Bischel, W. K. *Phys. Rev. A (Gen. Phys.)* **1986**, *34*, 185−98.
(16) Bamford, D. J.; Dyer, M. J.; Bischel, W. K. *Phys. Rev. A (Gen. Phys.)* **1987**, *36*, 3497−500.
(17) Eppink, A. T. J. B.; Parker, D. H. *Rev. Sci. Instrum.* **1997**, *68* 3477−3484.
(18) Yamanouchi, K.; Okunishi, M.; Endo, Y.; Tsuchiya, S. *J. Mol. Struct.* **1995**, *352/353*, 541.